

Vortex lattice states of bilayer electron-hole fluids in quantizing magnetic fields

Bo Zou and A.H. MacDonald

Department of Physics, University of Texas at Austin, Austin, TX 78712

(Dated: May 28, 2025)

We show that the ground state of a weakly charged two-dimensional electron-hole fluid in a strong magnetic field is a broken translation symmetry state with interpenetrating lattices of localized vortices and antivortices in the electron-hole-pair field. The vortices and antivortices carry fractional charges of equal sign but unequal magnitude and have a honeycomb lattice structure that contrasts with the triangular lattices of superconducting electron-electron-pair vortex lattices. We predict that increasing charge density or weakening magnetic field drives a vortex delocalization transition that would be signaled experimentally by an abrupt increase in counterflow transport resistance.

Introduction.— Recent progress [1–8] in separately contacting electrons and holes located in electrically isolated but nearby two-dimensional (2D) semiconductor layers has opened up new opportunities to study quasi-equilibrium electron-hole systems with separately tunable [9, 10] electron and hole densities. Because of the strong attractive interactions between electrons and holes, these systems have rich many-particle physics. In previous work we have discussed how electron-hole correlations are strengthened in strong magnetic fields when electron and hole densities are equal [11], leading to robust electron-hole-pair condensates that exhibit [7, 8] magnetic oscillations. Here we consider the case of a small but non-zero total charge density. We find that, instead of a Wigner crystal of unit charge quasiparticles, the ground state has a lattice of fractionally charged vortices and antivortices in the electron-hole-pair amplitude.

Vortex lattice states are common in systems with $U(1)$ order parameters. Common examples include the vortex lattices in type-II superconductors [12] in external magnetic fields and in rotating atomic superfluids[13]. In these systems, vortices are induced by magnetic fluxes and rotations respectively and the total vorticity is proportional to system size. Because vortices and antivortices can annihilate, lattice states with equal numbers of vortices and antivortices are less common, although they have been proposed as a theoretical possibility in both ^4He films and two-dimensional cold atoms [14, 15], and can be generated by periodic external potentials[16, 17] in polariton fluids. In lattice states with equal numbers of vortices and antivortices, the total vorticity vanishes. In the electron-hole fluids we discuss, vortices and antivortices carry electrical charges of the same sign so that repulsive Coulomb interactions disfavor annihilation.

In an electron-hole fluid at strong magnetic fields the lowest energy charged excitations are vortex or antivortex textures in the electron-hole-pair order-parameter field. They therefore appear in the ground state when a net charge density is induced by gate voltage settings. Unlike the charged Cooper pairs in superconductors, excitonic pairs do not accumulate Aharonov-Bohm phase by enclosing magnetic flux. Any net vorticity per unit area therefore has a large gradient energy cost, so that vortices

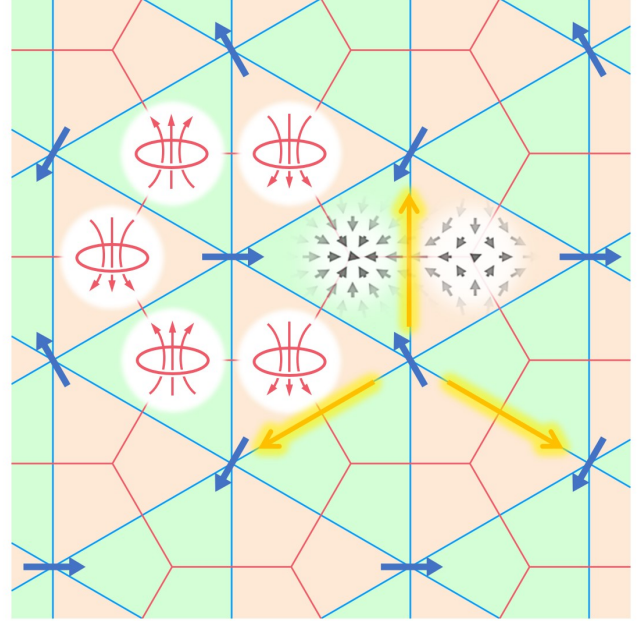


FIG. 1. Schematic illustration of the vortex lattice mean-field ground states of charged electron-hole fluids in a strong magnetic field. The vortices and antivortices form a honeycomb lattice with red links. The electron-hole pair amplitude vanishes at the vortex and antivortex centers and peaks on the triangular lattice sites whose links are marked in blue. Each peak is marked by a blue arrow representing the local condensate phase. Phases differ by $\frac{2\pi}{3}$ across the near-neighbor links marked by gold arrows, and by $-\frac{2\pi}{3}$ across links with opposite orientations. A Bose-Hubbard lattice model of this condensate contains alternating gauge fluxes in the green and orange triangles that originate from loop currents around vortices and antivortices.

and antivortices must have equal densities. The connection between charge-density and order-parameter texture closely parallels that of Skyrmion charged spin textures [18, 19] in quantum Hall ferromagnets and meron textures [20–22] in electron-electron bilayers in the quantum Hall regime. The charges hosted in the cores of a vortex and an antivortex sum to one elementary charge. When electrons or holes are added to a neutral condensate, they

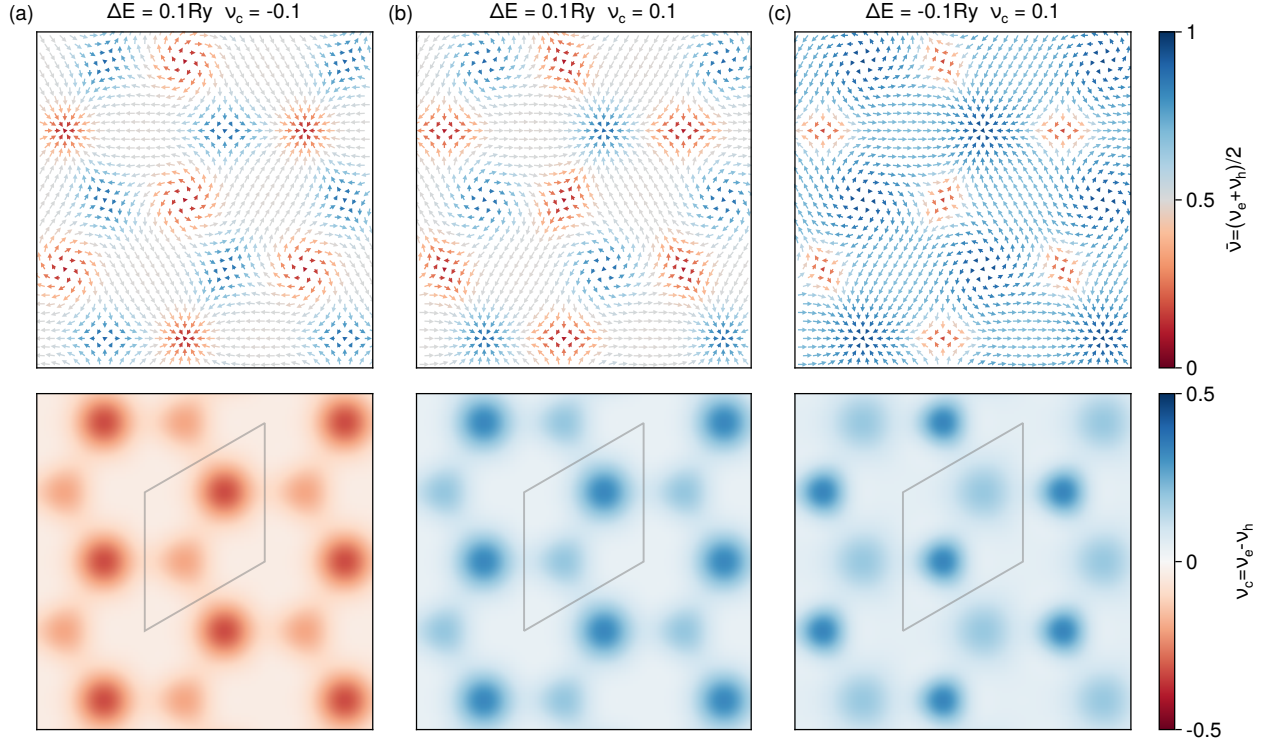


FIG. 2. Honeycomb-lattice exciton vortex lattice states at magnetic field $B = 0.1B_0$ and layer separation $d = a_B$ at different effective gap ΔE and average charge filling factor ν_c , where B_0 , a_B and Ry are the characteristic exciton magnetic field, length and energy scales defined in the main text. The lengths and orientations of the arrows represent the electron-hole-pair condensate magnitudes and phases, respectively, and the color scales represent the average (top) and the difference (bottom) of the electron and hole charge densities - both expressed as local Landau level filling factors. The comparison between (a) and (b) illustrates the particle-hole symmetry of our model whereas the comparison between (b) and (c) illustrates the dependence on the effective band gap ΔE . Four types of charged vortices, distinguished by vorticity and charge sign, appear as generalizations of the half-charged (meron) vortices in balanced electron bilayers. The charge density distribution is sensitive to the effective band gap ΔE , as discussed in the main text. These mean-field solutions were obtained at strong fields where Landau quantization is quite significant; results for weaker fields are illustrated in the supplementary material. The unit cell area (outlined in the bottom figures) of the broken translation symmetry state $A_{uc} = A_\Phi/|\nu_c|$, which includes one vortex and one antivortex, contains exactly one elementary charge.

fractionalize into vortex-antivortex pairs. Our calculations show that once many of these charged textures are present they crystallize into the honeycomb lattice arrangement illustrated in Fig. 1.

Charged Electron-Hole Bilayers in Strong Perpendicular Magnetic Fields— We consider electron and hole layers that are separately contacted with voltages $V_{e,h}$ in the geometry discussed in Refs. [1, 2, 6, 9–11] and in the supplementary material[23]. When the leakage current between two layers is negligible, the electrons and holes come to equilibrium with separate particle reservoirs and the system can be mapped to an equilibrium electron-hole system with separately conserved electron and hole numbers and an effective band gap $\Delta E = \epsilon_c - \epsilon_v + e(V_e - V_h)$. Dual-gating, isolation between layers, and separate-contacting make it possible in combination to realize two-dimensional electron-hole fluids in which the total charge density and the effective band gap

are separately electrically tunable, and electron-hole recombination processes are absent - eliminating many of the subtle complications that obscure many-particle interaction physics in optically pumped electron-hole systems.

We assume that a perpendicular magnetic field is present that is strong enough to permit truncation of both electron and hole Hilbert spaces to a finite number of Landau levels. For simplicity we also assume that both electrons and holes are fully spin-polarized by a combination of Zeeman and interaction effects, although this simplification is easily relaxed. Choosing the middle of the effective gap as the zero of energy and taking electron and hole masses m^* to be equal for definiteness, the Landau level energies in the conduction and valence bands are $\epsilon_{n,c/v} = \pm \frac{1}{2} \Delta E \pm (n + \frac{1}{2}) \hbar \omega_c$, where $\omega_c = eB/m^*c$ is the cyclotron frequency. Each Landau level has degeneracy $N_\Phi = A/A_\Phi$ with A being the sam-

ple area and $A_\Phi = hc/eB$ being the flux quantum area, so that carrier densities n and p are related to Landau level filling factors by $n(p) = \nu_{e(h)}/A_\Phi$. The total charge filling factor is defined as $\nu_c = \nu_e - \nu_h$.

Vortex Lattice States— We have previously discussed the strong field states of neutral electron-hole fluids ($\nu_c=0$), focusing on the competition between condensed and uncondensed phases induced by Landau kinetic energy quantization[11]. The uncondensed phases are integer quantum Hall phases in which both layers have fully occupied Landau levels. They appear only above critical magnetic field strengths beyond which large Landau level spacings suppress exciton-binding coherence and give rise to unusual quantum oscillation behavior in insulating states that has now been confirmed experimentally [7, 8]. To describe charged order-parameter-texture states, we solve unrestricted Hartree-Fock equations that account for Landau-level mixing and broken translation symmetry using a convenient equation of motion approach that takes advantage of the analyticity of the Landau-level wavefunctions to express Green's functions, density matrices, and Fock potentials in terms of Fourier transforms of local quantities, greatly simplifying the calculations. The technical details of these calculations are explained in the Supplementary Material [23]. We find that adding extra electrons or holes to the neutral exciton condensate leads to the honeycomb lattice [24] of vortices and antivortices described above. The Hartree-Fock equations also have uniform-density solutions in which the mean-field quasiparticles of the excitonic insulators accommodate the excess charge, but these have higher energy.

Fig. 2 illustrates the spatial variation of the electron and hole charge densities and the electron-hole-pair magnitude and phase for $d = a_B$ and $B = 0.1B_0$. (The exciton Bohr radius $a_B = 2\epsilon\hbar^2/e^2m^*$, the Rydberg energy $Ry = e^2/2\epsilon a_B$, and the characteristic magnetic field scale B_0 is defined by $a_B^2 B_0 = A_\Phi B$. [25].) At this field strength electrons and holes occupy mainly the lowest few Landau levels. In Fig. 2, the orientations and lengths of the arrows depict the electron-hole pair phase and magnitude and make the pattern of vortices and antivortices visible. The color scales indicate the sum and difference of the local electron and hole densities expressed as filling factors. The vortex lattice states in Figs. 2(a) and (b) are at the same gap $\Delta E = 0.1Ry$ but have opposite $\nu_c = \pm 0.1$. Because of the particle-hole symmetry of the theory, the two results differ only in the sign of the charge density and in the vorticity of the vortices. In total, we recognize four types of vortices [26] distinguished by their vorticity and fractional charge signatures, two of which appear on the electron side ($\nu_c > 0$) and two on the hole side ($\nu_c < 0$). On each side, the two realized vortices have opposite vorticities and fractional charges that are unequal in magnitude but alike in sign. In the lattice, the charged vortices contribute in combination one elementary charge per unit cell and have opposite

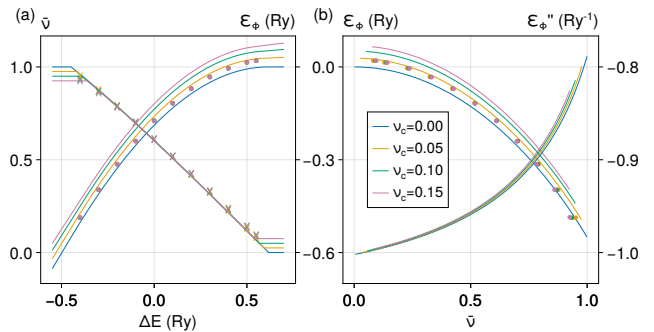


FIG. 3. (a) Ground state energy \mathcal{E}_Φ per A_Φ unit of area and average carrier filling factor $\bar{\nu}$ at $B=0.1B_0$, $d=a_B$ vs. ΔE . The energies are plotted as circles and the filling factors as crossings. The dependence on ν_c , indicated by color, is weak so that markers of different colors often overlap. The lines are data for uniform exciton condensates for reference. (b) \mathcal{E}_Φ and its second derivative with respect to ΔE are plotted vs. $\bar{\nu}$. The second derivative defines the interaction parameter U in the Bose-Hubbard lattice model approximation to the vortex solutions. (See the main text.)

layer polarizations in their core regions. The unit cell area is therefore $A_{uc} = A_\Phi/|\nu_c|$. Each vortex has three neighboring antivortices and vice versa. [27]

In Fig. 2(c), the effective gap ΔE has been lowered relative to that in Fig. 2(b). As a result the electron and hole densities are increased and the partitioning of the unit charge between the vortex and antivortex core regions is changed. By tuning ΔE , we can make the charge near one sublattice approach one while the charge near the other sublattice approaches zero so that the honeycomb vortex lattice states continuously evolve to triangular lattice electron or hole Wigner crystals[28]. As in the neutral case, in some intervals of ΔE either electrons or holes are at an integer filling factor and excitonic order is lost.

Quantum Fluctuations and Quantum Melting— To account for the role of the order-parameter quantum fluctuations, we construct a simplified lattice model that captures the essence of our microscopic results. We view the system as consisting of weakly linked condensate regions, centered on the triangular lattice sites marked by blue arrows in Fig. 1, described by a generalized Bose-Hubbard model Hamiltonian

$$H = \frac{U}{2} \sum_i \hat{n}_i(\hat{n}_i - 1) - J \sum_{\langle ij \rangle} (e^{iA_{ij}} b_j^\dagger b_i + h.c.), \quad (1)$$

where $\langle ij \rangle$ are nearest-neighbor sites, b_i^\dagger and b_i are exciton creation and annihilation operators on lattice site i and $\hat{n}_i = b_i^\dagger b_i$. In Eq. 1 A_{ij} is an emergent gauge field that we elaborate on below, U is the on-site exciton-exciton interaction, and J is the Josephson coupling between nearest neighbor condensate regions.

We estimate the strength of U by noticing that

$-\Delta E$ acts as a chemical potential for excitons so that the inverse short-range interaction strength satisfies $(UA_{ex})^{-1} = -\partial^2 \mathcal{E} / \partial \Delta E^2 = -\mathcal{E}''$ where \mathcal{E} is the ground state energy per area and A_{ex} is the area over which the excitons on a given lattice site are spread. A_{ex} is expected to be smaller than but close to $A_{uc} = |\nu_c|^{-1} A_\Phi$, implying that $U \sim -|\nu_c| / (\mathcal{E}'' A_\Phi)$. Using the mean-field results plotted in Fig. 3(b) we conclude that $U \sim |\nu_c| \text{ Ry}$ for $B = 0.1 B_0$ and $d = a_B$. The Josephson coupling is related to the stiffness of the continuum model [23] and is estimated as $J \sim 10^{-2} |\nu_c| \text{ Ry}$ for $B = 0.1 B_0$ and $d = a_B$. It follows that $J/U \sim 10^{-2}$ is independent of ν_c .

As illustrated in Fig. 1 and Fig. 2, the mean-field state has a pattern of phase variation that is induced by the vortices, making it different from the normal Bose-Hubbard model. The emergent gauge field A_{ij} is introduced so that the lattice-model superfluid state mimics the continuum HF results, *i.e.*, to induce the differences in exciton condensate phases between nearest-neighbor sites induced by the vortices and antivortices. In the three directions that we plot as gold arrows in Fig. 1, $A_{ij} = 2\pi/3$, and in the opposite directions, $A_{ij} = -2\pi/3$. The origin of the gauge field is that the currents around the vortices induce effective fluxes $+1$ in the green triangles associated with vortices and -1 in the orange triangles associated with antivortices, as illustrated in Fig. 1. The gauge fields simply shift the single-exciton bands rigidly in momentum space so that the excitons condense at K or $K' = -K$ (the two inequivalent corners of the Brillouin zone), depending on the sign of ν_c . The phase diagram associated with Eq. 1 is therefore identical to that of the normal Bose-Hubbard [29] model.

The superfluid/insulator phase boundary of the Bose-Hubbard model depends on the number of excitons per site $\langle n_i \rangle = \nu_{ex} / \nu_c$ and the ratio of Josephson coupling to interaction strength J/U . The vortex-lattice superfluid phase survives when J/U is larger than $\sim \langle n_i \rangle^{-1} \sim |\nu_c|$ [29]. We conclude that the vortex lattice states are stable at small $|\nu_c|$ but eventually melt at larger charge densities where quantum fluctuations destroy the superfluid order. Provided that the broken translation symmetry survives in this vortex-fluid state the resulting state could consist of a lattice of trions, or more generally of the multi-exciton charged complexes anticipated in Ref. [30]. We estimate that the critical charge filling factor is around 0.1 for $B = 0.1 B_0$ and $d = a_B$ and decreases with increasing magnetic field.

Discussion— In Fig. 4, we propose a schematic phase diagram for strong-magnetic-field states of weakly charged electron-hole fluids that goes beyond the vortex lattice (VL) and Wigner crystal (WC) states accessible in mean-field theory by accounting for competing (electron-hole plasmas (EHP), Bose-Fermi mixture (BFM), and fractional quantum Hall (FQH) states) expected to be stable in different extreme limits. In Fig. 4 we mark explicitly calculated phase boundaries by solid lines and

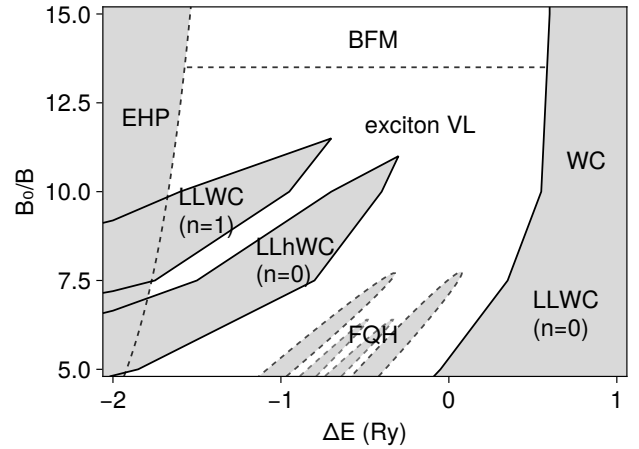


FIG. 4. Schematic phase diagram of a charged electron-hole fluid at a strong magnetic field B and small positive charge filling factors ν_c . The exciton density decreases when the electrically tunable effective band gap ΔE increases. At large positive ΔE , no excitons are present and the ground state is an electron Wigner crystal. At strong fields, layer-incoherent LLWC and LLhWC states with integer electron or hole filling factors interrupt the VL state and produce magnetic oscillations. Note that the Wigner crystal and vortex lattice states share the same lattice constants. The boundaries between these phases have been determined by performing unrestricted HF calculations with $\nu_c = 0.1$ and $d = a_B$ - and are plotted as solid lines. Phases anticipated in various extreme limits are also shown in this diagram along with estimated phase boundary positions (marked by dashed lines). Fractional incompressible states are anticipated under stronger magnetic fields if the sample is clean. A Mott transition to an electron-hole plasma (EHP) phase is expected at high densities of electrons and holes. In weaker fields, charge is not bound to exciton textures, making the crystal easier to melt. At both weaker fields and higher ν_c , we expect boson/fermion mixtures (BFM) (in either fluid or crystal states) that contain excitons and charged fermionic exciton complexes to compete. The white regions in this phase diagram have interlayer coherence.

phase boundaries expected due to beyond mean-field physics by dashed lines placed at crudely estimated positions. Fig. 4 extends the phase diagram in Ref. [11] from neutral to charged systems. If we assume that the excess charges are electrons, electron WC's form at all field strengths for large positive ΔE . The intermediate ΔE region is dominated by the exciton-condensate VL states on which we focus. These states are counterflow superfluids when vortices are pinned by weak disorder and should be easy to identify experimentally by large transport drag ratios. At small ΔE (larger exciton density), interlayer phase coherence is lost due to kinetic energy quantization when either ν_e or ν_h is an integer. The vortex lattice then evolves into Landau-level electron or hole Wigner crystal (LLWC/LLhWC) states in which the excess charges are accommodated by electron or hole

Wigner crystals in the partially filled Landau level. The Wigner crystals and vortex lattices have the same lattice constants. Higher-integer-filling (see [23]) versions of these states (not explicitly indicated in Fig. 4) are expected at smaller ΔE until the exciton density exceeds the Mott limit and EHP states emerge. Fractional-filling analogs of these states are expected in stronger fields in clean samples. At weaker fields, mixing of higher Landau levels is reflected in the spatial patterns of the electron-hole pair amplitude and charge density [23]. In the weak field limit, vortices do not appear in the ground state. In this regime we expect that Bose-Fermi mixture (BFM) fluids, and crystals composed of excitons and electrons, or trions and other multi-exciton-electron complexes[30] compete.

Our calculations point to the richness of charged electron-hole systems in the quantum Hall regime and motivate further experimental study. The large magnetic field scale B_0 for devices realized in TMD materials[1–8], which can be traced to their larger carrier effective masses, is the main obstacle to the experimental realization of the exciton-superfluid vortex lattice state. The strong field limit of our theory applies equally well to graphene electron-electron fluids near total filling factor 1,[31–33] where the required magnetic field scale is much smaller because of the large cyclotron frequency. Both vortex lattice and uniform density exciton condensates can support counterflow superfluidity. The vortex lattice state can be distinguished by counterflow-current-driven depinning transitions that allow vortices and antivortices to flow and provide a dissipation channel. Recent developments in scanning tunnel microscopy suggest that it might be possible to measure the spatial pattern of the vortex lattice directly.

Acknowledgements.— We thank Kin Fai Mak, Ruishi Qi, Jie Shan, Emanuel Tutuc and Feng Wang for helpful discussions. This work is supported by the Office of Naval Research under the Multidisciplinary University Research Initiatives (grant no. N00014-21-1-2377).

[1] L. Ma, P. X. Nguyen, Z. Wang, Y. Zeng, K. Watanabe, T. Taniguchi, A. H. MacDonald, K. F. Mak, and J. Shan, Strongly correlated excitonic insulator in atomic double layers, *Nature* **598**, 585 (2021).
 [2] J. Gu, L. Ma, S. Liu, K. Watanabe, T. Taniguchi, J. C. Hone, J. Shan, and K. F. Mak, Dipolar excitonic insulator in a moiré lattice, *Nature Physics* **18**, 395 (2022).
 [3] P. X. Nguyen, L. Ma, R. Chaturvedi, K. Watanabe, T. Taniguchi, J. Shan, and K. F. Mak, Perfect coulomb drag in a dipolar excitonic insulator, *Science* **388**, 274 (2025).
 [4] Y. Zeng, Z. Xia, R. Dery, K. Watanabe, T. Taniguchi, J. Shan, and K. F. Mak, Exciton density waves in coulomb-coupled dual moiré lattices, *Nature Materials* **22**, 175 (2023).

[5] R. Qi, A. Y. Joe, Z. Zhang, J. Xie, Q. Feng, Z. Lu, Z. Wang, T. Taniguchi, K. Watanabe, S. Tongay, *et al.*, Perfect coulomb drag and exciton transport in an excitonic insulator, *Science* **388**, 278 (2025).
 [6] R. Qi, A. Y. Joe, Z. Zhang, Y. Zeng, T. Zheng, Q. Feng, J. Xie, E. Regan, Z. Lu, T. Taniguchi, *et al.*, Thermodynamic behavior of correlated electron-hole fluids in van der waals heterostructures, *Nature communications* **14**, 8264 (2023).
 [7] P. X. Nguyen, R. Chaturvedi, B. Zou, K. Watanabe, T. Taniguchi, A. H. MacDonald, K. F. Mak, and J. Shan, Quantum oscillations in a dipolar excitonic insulator, arXiv preprint arXiv:2501.17829 (2025).
 [8] R. Qi, Q. Li, Z. Zhang, Z. Cui, B. Zou, H. Kim, C. Sanborn, S. Chen, J. Xie, T. Taniguchi, *et al.*, Competition between excitonic insulators and quantum hall states in correlated electron-hole bilayers, arXiv preprint arXiv:2501.18168 (2025).
 [9] M. Xie and A. H. MacDonald, Electrical reservoirs for bilayer excitons, *Physical review letters* **121**, 067702 (2018).
 [10] Y. Zeng and A. MacDonald, Electrically controlled two-dimensional electron-hole fluids, *Physical Review B* **102**, 085154 (2020).
 [11] B. Zou, Y. Zeng, A. H. MacDonald, and A. Strashko, Electrical control of two-dimensional electron-hole fluids in the quantum hall regime, *Physical Review B* **109**, 085416 (2024).
 [12] A. A. Abrikosov, Nobel lecture: Type-II superconductors and the vortex lattice, *Reviews of modern physics* **76**, 975 (2004).
 [13] A. L. Fetter, Rotating trapped bose-einstein condensates, *Reviews of Modern Physics* **81**, 647 (2009).
 [14] S.-C. Zhang, Vortex-antivortex lattice in superfluid films, *Physical review letters* **71**, 2142 (1993).
 [15] S. Botelho and C. Sá de Melo, Vortex-antivortex lattice in ultracold fermionic gases, *Physical review letters* **96**, 040404 (2006).
 [16] R. Hivet, E. Cancellieri, T. Boulier, D. Ballarini, D. Sanvitto, F. M. Marchetti, M. Szymanska, C. Ciuti, E. Giacobino, and A. Bramati, Interaction-shaped vortex-antivortex lattices in polariton fluids, *Physical Review B* **89**, 134501 (2014).
 [17] M. Milošević and F. Peeters, Vortex-antivortex lattices in superconducting films with magnetic pinning arrays, *Physical review letters* **93**, 267006 (2004).
 [18] S. L. Sondhi, A. Karlhede, S. Kivelson, and E. Rezayi, Skyrmions and the crossover from the integer to fractional quantum hall effect at small zeeman energies, *Physical Review B* **47**, 16419 (1993).
 [19] L. Brey, H. Fertig, R. Côté, and A. MacDonald, Skyrme crystal in a two-dimensional electron gas, *Physical review letters* **75**, 2562 (1995).
 [20] K. Yang, K. Moon, L. Zheng, A. MacDonald, S. Girvin, D. Yoshioka, and S.-C. Zhang, Quantum ferromagnetism and phase transitions in double-layer quantum hall systems, *Physical review letters* **72**, 732 (1994).
 [21] K. Moon, H. Mori, K. Yang, S. Girvin, A. MacDonald, L. Zheng, D. Yoshioka, and S.-C. Zhang, Spontaneous interlayer coherence in double-layer quantum hall systems: Charged vortices and kosterlitz-thouless phase transitions, *Physical Review B* **51**, 5138 (1995).
 [22] K. Yang, K. Moon, L. Belkhir, H. Mori, S. Girvin, A. MacDonald, L. Zheng, and D. Yoshioka, Spontaneous

- interlayer coherence in double-layer quantum hall systems: Symmetry-breaking interactions, in-plane fields, and phase solitons, *Physical Review B* **54**, 11644 (1996).
- [23] See supplementary material.
 - [24] In addition to the honeycomb lattice solutions, we also find square vortex lattice solutions of the Hartree-Fock equations, but their energies are higher and we do not discuss them here.
 - [25] For transition metal dichalcogenide (TMD) bilayers encapsulated by hexagonal boron nitride (hBN), $a_B \approx 1.3\text{nm}$, $Ry \approx 0.11\text{eV}$, and $B_0 \approx 2.4 \times 10^3\text{T}$, whereas for GaAs quantum well systems, which have smaller masses and larger dielectric constants, the corresponding scales are approximately 12nm , 4.8meV and 28T .
 - [26] For brevity, we use vortices to refer to all the vortex and antivortex objects where it does not cause ambiguity.
 - [27] Changing the sign of the magnetic field reverses the vorticity for a given sign of charge; in this letter we assume that the magnetic field is in the $+z$ direction, *i.e.*, $B = B_z > 0$.
 - [28] By hole Wigner crystals, on the electron doping side ($\nu_c > 0$), we refer to the crystal formed by orbitals unoccupied by holes in the valence band Landau levels. These quasiparticles have the same charge as electrons and will form Wigner crystals with the same period. See Ref.[34].
 - [29] M. P. Fisher, P. B. Weichman, G. Grinstein, and D. S. Fisher, Boson localization and the superfluid-insulator transition, *Physical Review B* **40**, 546 (1989).
 - [30] J. Palacios, D. Yoshioka, and A. MacDonald, Long-lived charged multiple-exciton complexes in strong magnetic fields, *Physical Review B* **54**, R2296 (1996).
 - [31] J. Li, T. Taniguchi, K. Watanabe, J. Hone, and C. Dean, Excitonic superfluid phase in double bilayer graphene, *Nature Physics* **13**, 751 (2017).
 - [32] X. Liu, K. Watanabe, T. Taniguchi, B. I. Halperin, and P. Kim, Quantum hall drag of exciton condensate in graphene, *Nature Physics* **13**, 746 (2017).
 - [33] K. A. Lin, N. Prasad, G. W. Burg, B. Zou, K. Ueno, K. Watanabe, T. Taniguchi, A. H. MacDonald, and E. Tutuc, Emergence of interlayer coherence in twist-controlled graphene double layers, *Phys. Rev. Lett.* **129**, 187701 (2022).
 - [34] A. MacDonald and D. Murray, Broken symmetry states for two-dimensional electrons in a strong magnetic field, *Physical Review B* **32**, 2291 (1985).
 - [35] A. MacDonald and S. Girvin, Density matrices for states in the lowest landau level of a two-dimensional electron gas, *Physical Review B* **38**, 6295 (1988).

SUPPLEMENTARY MATERIALS

Device geometry and electrostatic potential

The device geometry analyzed in the main text is shown in Fig.S1. Two semiconducting layers are doped with electrons and holes with densities n and p by connecting them to separate reservoirs with voltages V_e and V_h , respectively. The two layers are separated by a layer of hexagonal boron nitride (hBN) with a thickness d large enough that interlayer leakage currents can be neglected. Because of the opaque hBN barrier each layer comes to equilibrium with its own reservoir:

$$\begin{aligned} -e(V_e - \phi_e) &= \epsilon_c + \mu_e(n, p), \\ e(V_h - \phi_h) &= -\epsilon_v + \mu_h(n, p). \end{aligned} \quad (S1)$$

The electric potentials $\phi_{e,h}$ have been explicitly separated in these expressions because they are gate geometry dependent, and the many-body chemical potentials $\mu_{e,h}$ are measured from the conduction band bottom ϵ_c and the valence band top ϵ_v respectively.

Typically the top and bottom gates are separated by large distances d_e and d_h and held at the same voltage - which we choose as ground. For this geometry the electrostatic potential energy

$$\begin{aligned} -e\phi_e(n, p) &= \frac{4\pi e^2 d_e}{\epsilon} \frac{(d_h + d)(n - p) + dp}{d_e + d_h + d} \\ &\approx \frac{2\pi e^2}{\epsilon} [d_g(n - p) + dp], \\ e\phi_h(n, p) &= \frac{4\pi e^2 d_h}{\epsilon} \frac{(d_e + d)(p - n) + dn}{d_e + d_h + d} \\ &\approx \frac{2\pi e^2}{\epsilon} [d_g(p - n) + dn]. \end{aligned} \quad (S2)$$

The simplified versions of these equations assume $d_e = d_h = d_g \gg d$. Here, ϵ is the zz -element of the hBN

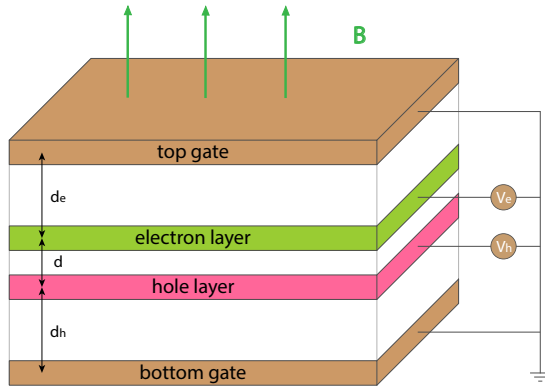


FIG. S1. Dual-gated device geometry.

dielectric constant. (We use the simplified formulas in the mean-field calculations explained in the following sections.) Note that the first term proportional to d_g is fixed by the charge density $n - p$ and can be neglected in finding the ground state. The second term corresponds to choosing $V(\mathbf{q} = 0) = 0$ for intralayer interactions $V(\mathbf{q} = 0) \sim -2\pi e^2 d/\epsilon$ for the $\mathbf{q} = 0$ interlayer electron-electron interactions. These choices are adopted below in Eq. S12. Although the term proportional to d_g is irrelevant in assessing the competition between competing states at a fixed charge density, it is responsible for the thermodynamic stability of the system, which requires that $\partial^2 E/\partial \nu_c^2 > 0$. Gate screening effects are important for small momentum $q < 1/d_g$. In our explicit calculations we assume that d_g is large enough that these can be neglected.

Hartree-Fock theory for electron-hole fluids in strong magnetic fields

We employ the Landau gauge, which is convenient for the description of crystal states, in our calculations. The states within a Landau level are therefore labeled by the guiding center positions on the x -axis X . For magnetic fields in the $+\hat{z}$ -direction, the corresponding wavefunctions are

$$\begin{aligned} \langle \mathbf{r} | n X \rangle &= \\ \frac{1}{\sqrt{2^n n! L_y}} \left(\frac{1}{\pi l^2} \right)^{\frac{1}{4}} e^{-\frac{1}{2} \left(\frac{x-X}{l} \right)^2 + i k_y y} H_n \left(\frac{x-X}{l} \right), \end{aligned} \quad (S3)$$

where n is the level index, $l = (\hbar c/eB)^{\frac{1}{2}}$ is the magnetic length and $k_y = -X/l^2$. The Landau gauge form factors

$$\begin{aligned} \langle n_1 X_1 | e^{i\mathbf{q} \cdot \mathbf{r}} | n_2 X_2 \rangle &= \\ F_{n_1, n_2}(\mathbf{q}) e^{i q_x \frac{X_1 + X_2}{2}} \delta_{X_1, X_2 - q_y l^2}, \end{aligned} \quad (S4)$$

where

$$\begin{aligned} F_{n_1, n_2}(q_x, q_y) &= F_{n_1, n_2}(q, \theta_{\mathbf{q}}) \\ &= \begin{cases} \sqrt{\frac{n_1!}{n_2!}} \left(\frac{i q_x - q_y l}{\sqrt{2}} \right)^{n_2 - n_1} \times \\ e^{-\frac{q^2 l^2}{4}} L_{n_1}^{(n_2 - n_1)} \left(\frac{q^2 l^2}{2} \right), & n_1 \leq n_2 \\ \sqrt{\frac{n_2!}{n_1!}} \left(\frac{i q_x + q_y l}{\sqrt{2}} \right)^{n_1 - n_2} \times \\ e^{-\frac{q^2 l^2}{4}} L_{n_2}^{(n_1 - n_2)} \left(\frac{q^2 l^2}{2} \right), & n_1 \geq n_2 \end{cases} \quad (S5) \\ &= \sqrt{\frac{n_{<}!}{n_{>}!}} \left(\frac{i q l}{\sqrt{2}} \right)^{n_{>} - n_{<}} e^{i \theta_{\mathbf{q}} (n_2 - n_1)} \times \\ &\quad e^{-\frac{q^2 l^2}{4}} L_{n_{<}}^{(n_{>} - n_{<})} \left(\frac{q^2 l^2}{2} \right), \end{aligned}$$

$(q, \theta_{\mathbf{q}})$ are the polar coordinates of \mathbf{q} , $n_>$ and $n_<$ are the larger and smaller integers among (n_1, n_2) , and $L_n^{(\alpha)}(x)$ is a generalized Laguerre polynomial. Note that $F_{n_1, n_2}(q_x = 0, q_y = 0) = \delta_{n_1, n_2}$. The momentum-space density operator is therefore

$$\begin{aligned} n_{bb'}(\mathbf{q}) &= \int d\mathbf{r} e^{-i\mathbf{q}\cdot\mathbf{r}} \psi_{b'}^\dagger(\mathbf{r}) \psi_b(\mathbf{r}) \\ &= \sum_{nn'} \sum_{XX'} \langle n' X' | e^{-i\mathbf{q}\cdot\mathbf{r}} | n X \rangle c_{b', n', X'}^\dagger c_{b, n, X} \quad (\text{S6}) \\ &= N_\Phi \sum_{nn'} \rho_{nn'}^{bb'}(\mathbf{q}) F_{n', n}(-\mathbf{q}). \end{aligned}$$

In Eq. S6, $b = c/v$ is the band/layer index, $N_\Phi = \Phi/\Phi_0$ is the number of states in each Landau level, and we have defined the Landau-level-resolved density operator $\rho_{bb'}^{nn'}(\mathbf{q})$ as

$$\rho_{bb'}^{nn'}(\mathbf{q}) = \frac{1}{N_\Phi} \sum_X e^{-iq_x(X + \frac{q_y}{2}l^2)} c_{b', n', X + q_y l^2}^\dagger c_{b, n, X}. \quad (\text{S7})$$

The prefactor $1/N_\Phi$ makes $\rho(\mathbf{q})$ an intensive quantity. Importantly Eq. S7 can be inverted:

$$c_{b', n', X'}^\dagger c_{b, n, X} = \sum_{\mathbf{q}} \delta_{X', X + q_y l^2} e^{iq_x \frac{X + X'}{2}} \rho_{nn'}^{bb'}(\mathbf{q}). \quad (\text{S8})$$

This remarkable formula implies that in the projected Hilbert space of any Landau level the position dependence of the charge density (the diagonal elements of the density matrix in a coordinate representation) uniquely determines the full density-matrix and therefore the Fock exchange potential. Below we use this property, which can be traced [35] to the analytic Hilbert-space of a single Landau-level, to simplify the Hartree-Fock calculations.

We define $V_{bb'}(\mathbf{q}) = 2\pi e^2 \exp(-qd(b, b'))/\epsilon q$ as the two-dimensional Fourier transform of the Coulomb energy between electrons in layers b and b' , separated by distance $d(b, b')$. With this notation the interaction Hamiltonian

$$\begin{aligned} V &= \frac{1}{2A} \sum_{bb'} \sum_{\mathbf{q}} \sum_{\substack{n_1, n_2, n_3, n_4 \\ X_1, X_2, X_3, X_4}} V_{bb'}(\mathbf{q}) \\ &\quad \langle n_1 X_1 | e^{-i\mathbf{q}\cdot\mathbf{r}} | n_4 X_4 \rangle \langle n_2 X_2 | e^{i\mathbf{q}\cdot\mathbf{r}} | n_3 X_3 \rangle \\ &\quad c_{b, n_1, X_1}^\dagger c_{b', n_2, X_2}^\dagger c_{b', n_3, X_3} c_{b, n_4, X_4}. \end{aligned} \quad (\text{S9})$$

Note that the layer indices are conserved at each vertex. Using Eq. S8 we find that the Hartree-Fock (HF) Hamiltonian can be expressed in terms of density operators:

$$\begin{aligned} H &= N_\Phi \sum_{nb} \epsilon_{n, b} \rho_{bb}^{nn}(\mathbf{q} = 0) + V \\ &= N_\Phi \sum_{nb} \epsilon_{n, b} \rho_{bb}^{nn}(\mathbf{q} = 0) \\ &\quad + N_\Phi \sum_{nn'} \sum_{bb'} U_{b'b}^{n'n}(\mathbf{q}) \rho_{nn'}^{bb'}(\mathbf{q}), \end{aligned} \quad (\text{S10})$$

where the coupling function U contains Hartree(H) and Fock/exchange(X) contributions, $U = U^H - U^X$, defined below. In these equations the density matrix is understood to be regularized by subtracting from it the full valence band density-matrix, $\delta_{bv} \delta_{bb'} \delta_{nn'} \delta_{\mathbf{q}0}$, since the single-particle energies implicitly include the self-energies they produce.

Both U^H and U^X are linear in the self-consistent density matrix $\langle \rho_{bb'}^{nn'}(\mathbf{q}) \rangle$. The Hartree contribution to U is diagonal in layer and involves only layer-diagonal density-matrix elements:

$$\begin{aligned} U_{b'b}^{n'n}(\mathbf{q}) &= U_{\bar{b}\bar{b}}^{n'n}(\mathbf{q}) \delta_{b, b'} \\ &= \frac{N_\Phi}{A} \delta_{b, b'} \sum_{mm'c} V_{bc}(\mathbf{q}) F_{n', n}(-\mathbf{q}) F_{m', m}(\mathbf{q}) \\ &\quad \times \langle \rho_{mm'}^{cc}(-\mathbf{q}) \rangle \quad (\text{S11}) \\ &= W_0 \delta_{b, b'} \sum_{mm'} \left(H_{nn'; mm'}(\mathbf{q}) \langle \rho_{mm'}^{bb}(-\mathbf{q}) \rangle \right. \\ &\quad \left. + H_{nn'; mm'}^*(\mathbf{q}) \langle \rho_{mm'}^{\bar{b}\bar{b}}(-\mathbf{q}) \rangle \right), \end{aligned}$$

where $W_0 = e^2/\epsilon l$ is the Coulomb energy scale, \bar{b} is the layer opposite to b , and the coefficients are given by

$$\begin{aligned} H_{nn'; mm'}(\mathbf{q} \neq 0) &= \frac{F_{n', n}(-\mathbf{q}) F_{m', m}(\mathbf{q})}{ql}, \\ H_{nn'; mm'}^*(\mathbf{q} \neq 0) &= \frac{F_{n', n}(-\mathbf{q}) F_{m', m}(\mathbf{q})}{ql} e^{-qd}, \\ H_{nn'; mm'}(0) &= 0, \\ H_{nn'; mm'}^*(0) &= \lim_{q \rightarrow 0} H_{nn'; mm'}^*(\mathbf{q}) - H_{nn'; mm'}(\mathbf{q}) \\ &= \delta_{nn'} \delta_{mm'} \frac{-d}{l}. \end{aligned} \quad (\text{S12})$$

Here the asterisk distinguishes interlayer from intralayer interaction contributions. As mentioned above, our treatment of Coulomb interaction energy at $\mathbf{q} = 0$ assumes that $d_g \gg d$ (see Eq. S2), and as explained previously leads to the convention that the same layer interaction $V_{bb}(0) = 0$.

The exchange contribution U^X has contributions that are off-diagonal in layer that are proportional to layer-off-diagonal density matrix components:

$$\begin{aligned} U_{b'b}^{Xn'n}(\mathbf{q}) &= \sum_{mm'} \int \frac{d\mathbf{k}}{(2\pi)^2} V_{bb'}(\mathbf{k}) F_{n', m}(-\mathbf{k}) F_{m', n}(\mathbf{k}) e^{i\mathbf{q} \times \mathbf{k} l^2} \\ &\quad \times \langle \rho_{mm'}^{b'b}(-\mathbf{q}) \rangle \quad (\text{S13}) \\ &= \begin{cases} W_0 \sum_{mm'} X_{nn'; mm'}(\mathbf{q}) \langle \rho_{mm'}^{b'b}(-\mathbf{q}) \rangle, & b = b' \\ W_0 \sum_{mm'} X_{nn'; mm'}^*(\mathbf{q}) \langle \rho_{mm'}^{b'b}(-\mathbf{q}) \rangle, & b = \bar{b}' \end{cases} \end{aligned}$$

Defining

$$\begin{aligned} s_1 &= m' - n, \quad n_{1>} = \max\{m', n\}, \quad n_{1<} = \min\{m', n\}, \\ s_2 &= n' - m, \quad n_{2>} = \max\{n', m\}, \quad n_{2<} = \min\{n', m\}, \end{aligned}$$

the coefficients X and X^* are given by

$$\begin{aligned} X_{nn';mm'}(q, \theta_{\mathbf{q}}) &= i^{|s_1|-|s_2|} e^{-i(s_1+s_2)\theta_{\mathbf{q}}} \\ &\times \sqrt{\frac{n_{1<}! n_{2<}!}{n_{1>}! n_{2>}!}} \int_0^\infty e^{-\frac{x^2}{2}} \left(\frac{x^2}{2}\right)^{\frac{1}{2}(|s_1|+|s_2|)} \\ &L_{n_{1<}}^{(|s_1|)} \left(\frac{x^2}{2}\right) L_{n_{2<}}^{(|s_2|)} \left(\frac{x^2}{2}\right) J_{s_1+s_2}(qlx) dx, \end{aligned} \quad (\text{S14})$$

$$\begin{aligned} X_{nn';mm'}^*(q, \theta_{\mathbf{q}}) &= i^{|s_1|-|s_2|} e^{-i(s_1+s_2)\theta_{\mathbf{q}}} \\ &\times \sqrt{\frac{n_{1<}! n_{2<}!}{n_{1>}! n_{2>}!}} \int_0^\infty e^{-\frac{x^2}{2} - x\frac{d}{l}} \left(\frac{x^2}{2}\right)^{\frac{1}{2}(|s_1|+|s_2|)} \\ &L_{n_{1<}}^{(|s_1|)} \left(\frac{x^2}{2}\right) L_{n_{2<}}^{(|s_2|)} \left(\frac{x^2}{2}\right) J_{s_1+s_2}(qlx) dx, \end{aligned} \quad (\text{S15})$$

where the $J_n(x)$ are Bessel functions of the first kind. Two properties

$$\begin{aligned} X_{m'm;n'n}^{(*)}(\mathbf{q}) &= [X_{nn';mm'}^{(*)}(\mathbf{q})]^* \\ X_{mm';nn'}^{(*)}(\mathbf{q}) &= X_{nn';mm'}^{(*)}(-\mathbf{q}) \end{aligned} \quad (\text{S16})$$

are useful in reducing the number of integrals that have to be evaluated numerically; the first ensures that the Hamiltonian is Hermitian, and the second originates from invariance of the Coulomb interaction under interchange of particle indices. The energy per flux quantum

$$\begin{aligned} \mathcal{E}_\Phi &= \frac{\langle H \rangle}{N_\Phi} = \sum_{nb} \epsilon_{n,b} \langle \rho_{nb}^{nn}(\mathbf{q}=0) \rangle \\ &+ \frac{1}{2} \sum_{nn'bb'} \sum_{\mathbf{q}} U_{n'n}^{bb'}(\mathbf{q}) \langle \rho_{bb'}^{nn'}(\mathbf{q}) \rangle, \end{aligned} \quad (\text{S17})$$

and energy per area is $\mathcal{E} = \mathcal{E}_\Phi / A_\Phi$.

Equation-of-motion Hartree-Fock solution

We define the momentum space Matsubara Green's functions as

$$\begin{aligned} G_{bb'}^{nn'}(\mathbf{q}; \tau) &= \frac{1}{N_\Phi} \sum_X e^{-iq_x(X + \frac{1}{2}q_y l^2)} \times \\ &\langle T [c_{b',n',X+q_y l^2}^\dagger(0) c_{b,n,X}(\tau)] \rangle \end{aligned} \quad (\text{S18})$$

has the same form as the density operator in Eq. S7. Here the imaginary-time creation and annihilation operators $c_{b,n,X}^{(\dagger)}(\tau) = e^{\tau(H-\mu N)} c_{b,n,X}^{(\dagger)} e^{-\tau(H-\mu N)}$, where μ is the chemical potential and T indicated time-ordering. The

commutator of an annihilation operator with the density operator

$$\begin{aligned} [\rho_{nn'}^{bb'}(\mathbf{q}), c_{c,m,X}] &= \\ &= -\frac{1}{N_\Phi} e^{-iq_x(X - \frac{1}{2}q_y l^2)} c_{b,n,X-q_y l^2} \delta_{b'c} \delta_{n'm}. \end{aligned} \quad (\text{S19})$$

It follows that the commutator with the Hamiltonian in Eq. S10

$$\begin{aligned} [H - \mu N, c_{c,m,X}] &= - \sum_{nb} (\epsilon_{n,b} - \mu) c_{c,m,X} \\ &- \sum_{nb} \sum_{\mathbf{k}} U_{mn}^{cb}(\mathbf{k}) e^{-ik_x(X - \frac{1}{2}k_y l^2)} c_{b,n,X-k_y l^2}. \end{aligned} \quad (\text{S20})$$

and that

$$\begin{aligned} &\hbar \frac{d}{d\tau} G_{bb'}^{nn'}(\mathbf{q}; \tau) \\ &= \frac{1}{N_\Phi} \sum_X e^{-iq_x(X + \frac{1}{2}q_y l^2)} \times \\ &\left[-\hbar \delta(\tau) \left\{ c_{b',n',X+q_y l^2}^\dagger, c_{b,n,X} \right\} \right. \\ &\left. \left\langle T c_{b',n',X+q_y l^2}^\dagger(0) [H - \mu N, c_{b,n,X}](\tau) \right\rangle \right] \\ &= -\hbar \delta(\tau) \delta_{bb'} \delta_{nn'} \delta_{\mathbf{q}0} - (\epsilon_{n,b} - \mu) G_{bb'}^{nn'}(\mathbf{q}; \tau) \\ &- \sum_{mc,\mathbf{k}} U_{mn}^{cb}(\mathbf{k}) e^{i\frac{1}{2}\mathbf{k} \times \mathbf{q} l^2} G_{cb'}^{mn'}(\mathbf{q} + \mathbf{k}; \tau), \end{aligned} \quad (\text{S21})$$

After Fourier transforming to Matsubara frequencies, we obtain

$$\begin{aligned} &(i\omega_n + \frac{\mu}{\hbar}) G_{bb'}^{nn'}(\mathbf{q}; i\omega_n) \\ &- \sum_{mc,\mathbf{q}'} A_{bc}^{nm}(\mathbf{q}, \mathbf{q}') G_{cb'}^{mn'}(\mathbf{q}'; i\omega_n) = \delta_{bb'} \delta_{nn'} \delta_{\mathbf{q}0}, \end{aligned} \quad (\text{S22})$$

where

$$\begin{aligned} \hbar A_{bc}^{nm}(\mathbf{q}, \mathbf{q}') &= \\ &\epsilon_{n,b} \delta_{nm} \delta_{bc} \delta_{\mathbf{q}\mathbf{q}'} + U_{bc}^{nm}(\mathbf{q}' - \mathbf{q}) e^{i\frac{1}{2}\mathbf{q}' \times \mathbf{q} l^2} \end{aligned} \quad (\text{S23})$$

is a Hermitian matrix which we diagonalize numerically:

$$\sum_{mc,\mathbf{q}'} A_{bc}^{nm}(\mathbf{q}, \mathbf{q}') V_{cm}^{(j)}(\mathbf{q}') = \omega^{(j)} V_{bn}^{(j)}(\mathbf{q}). \quad (\text{S24})$$

It follows that the Green's function is

$$G_{bb'}^{nn'}(\mathbf{q}; i\omega_n) = \sum_j \frac{V_{bn}^{(j)}(\mathbf{q}) [V_{b'n'}^{(j)}(0)]^*}{i\omega_n + \mu/\hbar - \omega^{(j)}}. \quad (\text{S25})$$

and that the self-consistent field equation for the density-matrix is

$$\begin{aligned} \langle \rho_{bb'}^{nn'}(\mathbf{q}) \rangle &= \lim_{\tau \rightarrow 0^-} G_{bb'}^{nn'}(\mathbf{q}; \tau) - \delta_{bv} \delta_{bb'} \delta_{nn'} \delta_{\mathbf{q}0} \\ &= \sum_j n_F(\hbar\omega^{(j)} - \mu) V_{bn}^{(j)}(\mathbf{q}) [V_{b'n'}^{(j)}(0)]^* \\ &- \delta_{bv} \delta_{bb'} \delta_{nn'} \delta_{\mathbf{q}0}, \end{aligned} \quad (\text{S26})$$

where n_F is the Fermi-Dirac distribution function, and the chemical potential μ is determined by the filling factor

$$\nu_c = \sum_{bn} \langle \rho_{bb}^{nn}(0) \rangle. \quad (\text{S27})$$

Broken Translational Symmetry

The previous sections explain the basic equations we use to solve unrestricted Hartree-Fock equations for an electron-hole fluid in a Landau level basis. The formulation of Hartree-Fock theory is unusual and takes advantage of the analyticity of the wavefunctions within each Landau level. Because we express the Hartree-Fock equations in terms of charge-density Fourier components $\langle \rho_{bb'}^{nn'}(\mathbf{q}) \rangle$, we can find broken translational-symmetry solutions with any lattice periodicity by allowing these to be non-zero only on the corresponding reciprocal lattice of momenta \mathbf{q} . Since the Hamiltonian is translationally invariant, non-zero $\langle \rho_{bb'}^{nn'}(\mathbf{q}) \rangle$ at any non-zero \mathbf{q} signals a broken symmetry. Layer-diagonal density-matrix elements are related to charge density fluctuations whereas layer-off-diagonal elements define the real-space pattern of interlayer excitonic coherence.

If we allow $\langle \rho_{bb'}^{nn'}(\mathbf{q}) \rangle$ to be non-zero only at $\mathbf{q} = 0$, both the charge and the exciton order parameter are uniform in real space. The vortex lattice solutions we find at small finite ν_c (small electron-hole imbalance) restrict \mathbf{q} to a reciprocal lattice corresponding to one charge per unit cell. We also find uniform solutions by restricting momenta to $\mathbf{q} = 0$, but these competitors to the vortex lattice states turn out to always have higher energy, as reported in Fig.(3) in the main text. Because the charge densities and excitonic order parameters are smooth functions of position we can cut-off the number of shells of the reciprocal lattice vectors. Our calculations do not assume that vortices and antivortices are present or that they have any particular spatial pattern when present, only that the solutions that we find are period. We can find solutions for any lattice type, but we find that the honeycomb lattice solutions discussed in the main text are lowest in energy.

The ground state solutions discussed in the main text have zero total counterflow supercurrent. We have also found solutions with finite supercurrent by simultaneously shifting the allowed momenta by \mathbf{Q} relative to reciprocal lattice vectors for ρ_{cv} and by $-\mathbf{Q}$ for ρ_{vc} . This transformation finds excitons with lattice momentum \mathbf{Q} . We have carried out calculations of this type for both uniform and vortex lattice ground states and used them to determine the exciton superfluid density discussed in the next section.

To solve the Hartree-Fock equations, we use a trial density matrix to construct the Greens function, and diagonalize it to obtain an updated density matrix. This

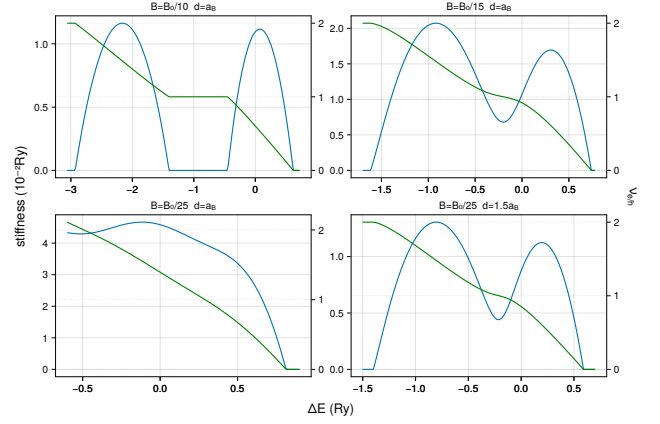


FIG. S2. The exciton condensate stiffness (blue) and carrier filling factor (green) at neutrality *vs.* band gap ΔE .

procedure is repeated until convergence is reached. Once the density matrix is converged, we calculate the corresponding energy and, by inverting the Fourier transform in Eq. S6, real space observables. Each iteration contains the following steps: (a) Calculate the mean field U using Eq. S11 and S13 and a weighted average of the input and output density matrices of the previous iteration (b) Find the A matrix using Eq. S23; (c) Diagonalize the A matrix and find its eigenvalues ω^j and eigenvectors V^j ; (d) Calculate the new density matrix ρ_{new} with ω and V using Eq. S26 with μ determined by ν_c .

Exciton superfluid density and the Josephson junction model hopping parameter

For the stiffness calculation we shift the interlayer coherence momenta by $\pm \mathbf{Q}$ as explained in the previous equations. The Hartree-Fock equation solutions can be solved for any value of $\pm \mathbf{Q}$ in the Brillouin-zone of the vortex lattice state. The main text focuses on the lowest energy solutions with coherence momentum $\pm \mathbf{Q} = 0$, and the expansion of the energy at small momentum is isotropic to quadratic order for triangular vortex lattices. The exciton stiffness s of the electron-hole condensate may be defined as the coefficient of the quadratic term in the small Q expansion of the condensate energy per area:

$$\mathcal{E}(Q) = \mathcal{E}(0) + sQ^2 + \dots \quad (\text{S28})$$

Fig. S2 plots the stiffness of neutral exciton condensates as blue lines, along with the exciton filling factor, as green lines. The stiffness is proportional to the superfluid density ν_{ex} . In strong fields, it reaches a maximum at half-filling of each Landau level, *i.e.* when $\nu_{ex} = 0.5$.

The tight-binding kinetic part of the effective Bose-

Hubbard model (eq. 1 in the main text) is

$$H = -J \sum_{\langle ij \rangle} (e^{iA_{ij}} b_j^\dagger b_i + h.c.) \quad (\text{S29})$$

gives the exciton band dispersion

$$E_Q = -2J \sum_{i=1}^3 \cos(\mathbf{Q} \cdot \mathbf{a}_i + A(\mathbf{a}_i)), \quad (\text{S30})$$

where $\mathbf{a}_{1,2,3}$ are three lattice vectors from the first shell with 120-degree relative angles and $A(\mathbf{a}_i)$ is the hopping phase gained from the gauge field. In neutral condensates, $A(\mathbf{a}_i) = 0$ and the band reaches its minimum at $\mathbf{Q} = 0$:

$$E_Q = E_0 + \frac{\sqrt{3}JA_\Phi}{|\nu_c|} Q^2 + \dots \quad (\text{S31})$$

Therefore, if the excitons are Bose condensed, the total energy per area

$$\mathcal{E}(Q) = E_Q \frac{\nu_{ex}}{A_\Phi} = \mathcal{E}(0) + \frac{\sqrt{3}J\nu_{ex}}{|\nu_c|} Q^2 + \dots \quad (\text{S32})$$

Comparing eq. S28 and S32, we conclude that we should

choose

$$J = \frac{|\nu_c|}{\sqrt{3}\nu_{ex}} s \quad (\text{S33})$$

in the lattice model.

Extended Results: Higher Landau-level solutions

At strong B or at smaller values of ΔE , we find model-parameter regions in which the Wigner crystal and vortex lattice states we find involve either many Landau levels or order that is associated mainly with $n > 0$ Landau levels. In Fig. S3, we illustrate the spatial patterns of the pairing amplitudes and charge densities in Wigner crystal and vortex lattice states at several points in the $(\Delta E, B)$ parameter space outside the regions focused on in the main text. Because higher Landau levels form factors play an important role in these solutions, the pairing and charge density patterns have more structure. In some cases the condensate regions A_{ex} between vortices shrink, implying that the interaction parameter U in our Bose-Hubbard lattice should increase - increasing the strength of quantum phase fluctuations.

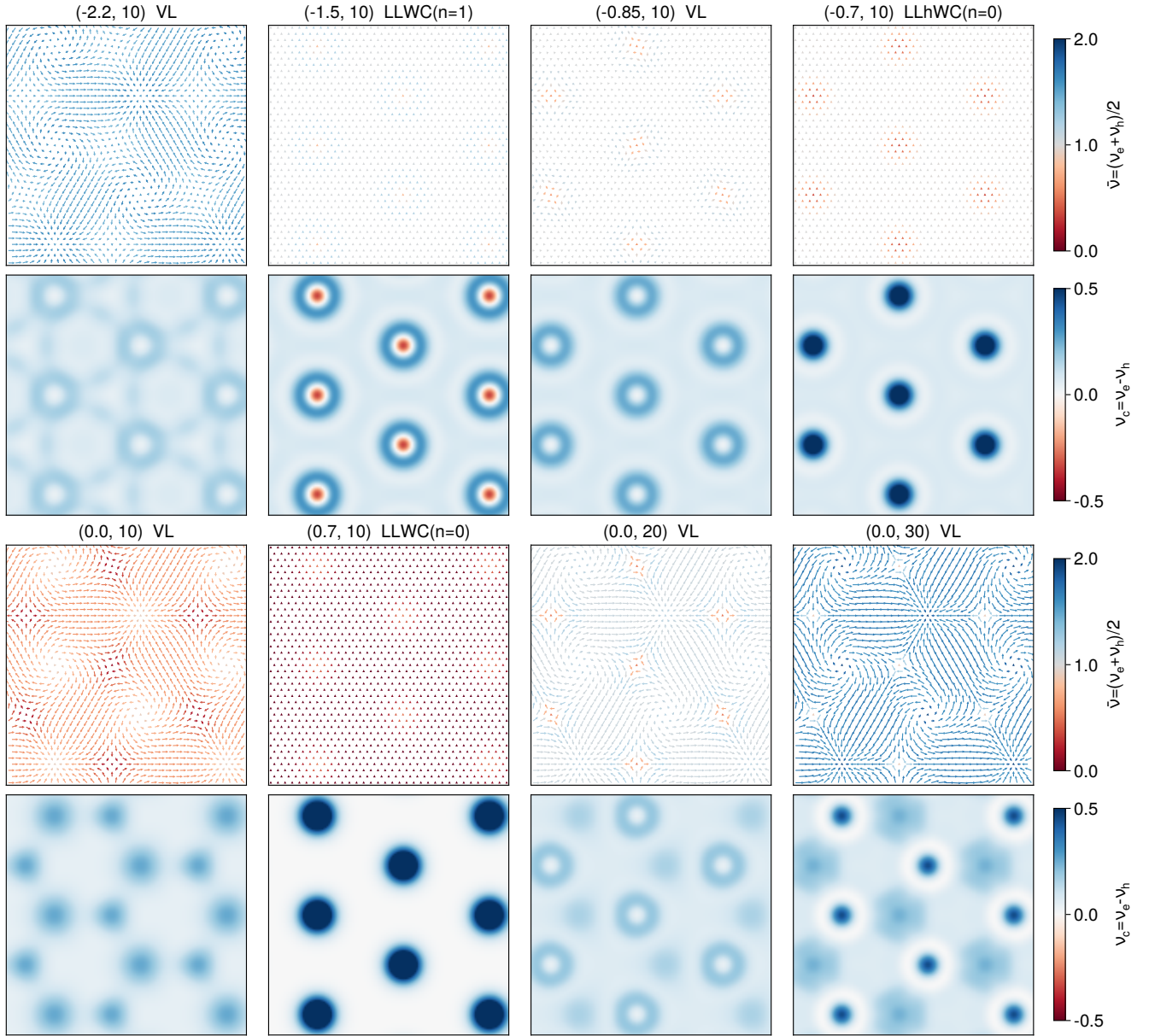


FIG. S3. Hartree-Fock calculation result summaries at eight additional $(\Delta E/Ry, B_0/B)$ values at $d = a_B$. For each value, the upper panel illustrates the pairing amplitude and phase and the bottom panel charge density. The layout of these figures is similar to that of Fig 2 in the main text. The HF solutions at these points correspond to vortex lattice (VL), Landau-level Wigner crystal (LLWC) and Landau-level-hole Wigner crystal (LLhWC) states as discussed in the main text. For Wigner crystal states in which interlayer coherence is absent, the pairing amplitudes and therefore the length of arrows are identically zero.